

Formation of Wide Binaries by Turbulent Fragmentation

Jeong-Eun Lee¹, Seokho Lee¹, Michael Dunham², Ken'ichi Tatematsu³, Minhoo Choi⁴, Edwin A. Bergin⁵, & Neal J. Evans II^{4,6}

¹*School of Space Research, Kyung Hee University, 1732, Deogyong-Daero, Giheung-gu, Yongin-shi, Gyunggi-do 17104, Korea*

²*State University of New York at Fredonia, Fredonia, 280 Central Ave., NY 14063, USA*

³*National Astronomical Observatory of Japan, 2-21-1 Osawa, Mitaka, Tokyo 181-8588, Japan*

⁴*Korea Astronomy and Space Science Institute, 776 Daedeokdae-ro, Yuseong-gu, Daejeon, 34055, Korea*

⁵*Department of Astronomy, University of Michigan, 500 Church St., Ann Arbor, MI 48109, USA*

⁶*Department of Astronomy, The University of Texas at Austin, 2515 Speedway, Stop C1402, Austin, TX 78712, USA*

Understanding the formation of wide binary systems of very low mass stars ($M \leq 0.1 M_{\odot}$) is challenging¹⁻³. The most obvious route is via widely separated low-mass collapsing fragments produced through turbulent fragmentation of a molecular core^{4,5}. However, close binaries/multiples from disk fragmentation can also evolve to wide binaries over a few initial crossing times of the stellar cluster through tidal evolution⁶. Finding an isolated low mass wide binary system in the earliest stage of formation, before tidal evolution could occur, would prove that turbulent fragmentation is a viable mechanism for (very) low mass wide binaries. Here we report high resolution ALMA observations of a known wide-separation

protostellar binary, showing that each component has a circumstellar disk. The system is too young⁷ to have evolved from a close binary and the disk axes are misaligned, providing strong support for the turbulent fragmentation model. Masses of both stars are derived from the Keplerian rotation of the disks; both are very low mass stars.

The two main theoretical formation mechanisms for multiple stars are turbulent fragmentation and disk fragmentation. These mechanisms result in different distributions of companion separations; wide (separation > 500 AU) binaries naturally form through turbulent fragmentation⁸, and close binaries form through disk fragmentation⁹. However, dynamical processes such as three-body interactions, radial migrations, and interactions with cluster members^{6,8,10} can turn initially close binaries into wide binaries. Therefore, in order to demonstrate formation by turbulent fragmentation, it is crucial to observe protostellar binary or multiple systems, which are younger than 0.5 Myrs, the timescale of the embedded protostellar phase¹¹, and thus, can reveal their initial configurations.

A survey of protostars in the Perseus molecular cloud found a bi-modal distribution of companion separations with a peak at 75 AU and another at 3000 AU¹². Therefore, evidence exists for both modes of binary formation. In addition, recent high resolution observations isolate specific targets to support each formation mechanism. Compelling evidence for disk fragmentation was revealed by a triple protostellar system forming in a common protostellar disk¹³. On the other hand, a quadruple condensation system was discovered and the authors claimed that it is evolving into a stellar system with a wide separation¹⁴; however, this system has so far formed only one protostar,

and its ultimate outcome is unclear.

Although the systems with larger separations are plausible candidates for formation by turbulent fragmentation, confirmation of this possibility requires further evidence, *the misalignment of rotation axes* of stars, disks, and outflows¹⁵. Turbulent fragmentation generates binaries with misaligned rotation axes because the angular momentum distribution in a turbulent core is random⁸. By contrast, binaries with aligned rotation axes ($\leq 20^\circ$)¹⁵ are predicted if the secondary member is formed in a large co-rotating massive disk/ring around the primary¹⁶ or if they are formed through the fragmentation driven by the centrifugal force in a flattened cloud core. Protostellar rotational axes are difficult to measure, but the bipolar outflow driven by a star-disk system can be used to test the alignment of angular momentum in the system¹⁵. However, outflow studies suffer from environmental effects¹⁷ or interactions between multiple outflows. A better indicator is the misalignment of disk rotation axes, but disk rotation axes of wide binaries have been reported only in the T-Tauri stage (more evolved than the protostellar stage)^{18–21}, which suffer from tidal evolution effects.

IRAS 04191+1523 is a known protostellar binary system with a projected separation of $6''.1$ (~ 860 AU) between members²² in Taurus, whose distance is 140 pc. Both companion protostars are in the early embedded evolutionary stage of Class I^{7,23}. The primary (protostar A) has a luminosity of $0.6 L_\odot$, and the secondary (protostar B) has $0.04 L_\odot$ ^{22,24,25}. Based on their luminosities, the secondary was considered as a candidate proto-brown dwarf²⁶. However, the protostellar luminosity is dominated by accretion luminosity, which depends on both stellar mass and accretion

rate. The only accurate way to compute protostellar masses is to observe Keplerian rotation²⁷.

IRAS 04191+1523 was observed with ALMA simultaneously in the 1.3 mm continuum and the C¹⁸O (J=2–1) emission on 4 January 2015, with $\sim 1.5''$ resolution. The 1.3 mm continuum was re-observed with ALMA, obtaining better resolution ($\sim 0.2''$) on 28 September 2016. The ALMA observations (Figure 1) at the lower resolution reveal two compact continuum sources, one for each protostar, connected by a bridge of emission in C¹⁸O. The C¹⁸O gas bridge and the same central velocities inferred from the C¹⁸O spectra over the elongated feature show that the two protostars belong to a single star-forming cloud core. The Herschel/PACS images²⁶ show a single core, flattened along the this C¹⁸O emission bridge, with a size of 0.02 pc, demonstrating sub-fragmentation within an isolated core.

The two continuum sources were resolved only in the higher resolution image (Figure 2). In the unresolved images (upper panel of Figure 3), the total continuum fluxes are $52.6 (\pm 1.6)$ mJy and $87.1 (\pm 2.0)$ mJy for protostars A and B, respectively. In the resolved images (lower panel of Figure 3), they are $53.5 (\pm 1.1)$ mJy and $71.1 (\pm 3.2)$ mJy for protostars A and B, respectively. The agreement between continuum fluxes from the two resolution images of protostar A indicates that the continuum sources are disks. On the other hand, the difference in flux between the two different images of protostar B indicates that no more than 20% (16/87) can be attributed to an envelope. We assume that the flux from the disk is 71.1 mJy as measured from the higher resolution image.

We use the higher resolution continuum image to derive the physical parameters of the continuum sources; the continuum comes from the thermal radiation of dust and provides the masses

of circumstellar material. Each of the dust continuum sources has the size and mass of a typical protostellar accretion disk (see Methods). The projected position angles of two disks derived from the dust continuum emission are significantly different by 55 ± 5 degrees (Supplementary Table 1), indicative of misaligned disk axes.

Since the gaseous disks are resolved even at the lower resolution, the C^{18}O emission provides information on the kinematics of the disks; the C^{18}O emission associated with each disk shows a velocity shift from one end of the disk to the other end, indicating rotation (Figure 3). In the red-shifted and blue-shifted velocity components together, the velocity shift is consistent with a Keplerian rotation profile (see Methods). Figure 4 presents the best-fit Keplerian rotation velocity profile in the peak-position-velocity diagram of each source; the position of the emission peak is found by Gaussian fitting of the emission distribution along the white line in Figure 3 for a given velocity. The minimum masses of the central objects (the protostars) can be derived from the best-fit models of these peak-position-velocity diagrams. Protostar A and B both have $M_* = 0.09 M_\odot$, assuming edge-on disks (see Supplementary Table 3). If the disk has an intermediate inclination, the corresponding mass should be scaled by $1/\sin^2 i$, where i is the inclination angle ($i = 90^\circ$ for edge-on disk). The aspect ratio of deconvolved continuum source size suggests the inclination angles of 55° and 59° for the disks of protostars A and B, respectively (see Methods). Therefore, the masses after correction for the inclinations are ~ 0.14 and $0.12 M_\odot$, which are close to the criterion of very low mass star ($M_* \leq 0.1 M_\odot$).

Protostar B cannot be substellar, unlike what would be expected from its very low luminosity²⁶.

Assuming that most of the luminosity comes from the mass accretion onto the protostars and protostellar radii are $2R_{\odot}$, the accretion rate of protostar A ($\dot{M} \sim 2.8 \times 10^{-7} M_{\odot}\text{yr}^{-1}$) is greater than that of protostar B ($\dot{M} \sim 2.1 \times 10^{-8} M_{\odot}\text{yr}^{-1}$) by a factor of ~ 13 . The current protostellar masses are similar to those of very low-mass stars, but they may grow by further accretion from the disks and envelope. Assuming a dust temperature of 30 K and a gas-to-dust mass ratio of 100, the disk masses are $(3.70 \pm 0.08) \times 10^{-3} M_{\odot}$ and $(4.91 \pm 0.22) \times 10^{-3} M_{\odot}$ for protostars A and B, respectively (see Methods). These disks cannot substantially increase the central masses. The total mass of the protostellar envelope is $0.1 M_{\odot}$ ²⁸. Assuming that 30%–50% of the envelope mass eventually winds up in the protostars¹¹, the future contribution from the envelope may be $\sim 0.04 M_{\odot}$. Consequently, the protostars cannot grow very much, and the final configuration is likely to be a pair of low mass stars separated by at least 1000 AU. If the accretion rate of protostar A stays much larger than that of protostar B even in the future, the primary mass will be about $0.18 M_{\odot}$, which is not much bigger than the secondary mass ($0.12 M_{\odot}$).

From Kepler’s third law, with the total mass of $0.26 M_{\odot}$, the orbital period of the binary system is $\sim 5 \times 10^4 (\pm 5.5 \times 10^3)$ years if we consider the projected separation (860 AU) as the actual separation between companions; the dominant error of orbital period is the distance error, which is about 10 pc. If the separation on the plane of sky is the same as the separation along the line of sight, the actual separation is $\sqrt{2}$ times the projected separation, and the orbital period becomes 0.1 Myr. A significant change of system configuration by tidal interactions would take a time much longer than the orbital period. The age of IRAS 04191+1523 is about 0.1 Myr in the assumption of a typical protostellar accretion rate of $10^{-6} M_{\odot}\text{yr}^{-1}$ and the protostellar mass

of $0.1 M_{\odot}$. Its age should not exceed the timescale (0.5 Myr) of the protostellar phase¹¹. The similarity between the envelope and each protostellar mass indicates that IRAS 04191+1523 is a relatively young Class I source²⁹. Therefore, the orbital period of the IRAS 04191+1523 system is comparable with its age, and this binary system should still be in its initial configuration.

The projected disk rotation axes are perpendicular to the white lines over two gaseous disks in Figure 3, which are misaligned by 77° (see Methods), indicating that they formed via turbulent fragmentation since this binary is too young to modify the alignment of rotational axes by tidal interactions between companions¹⁵. The derived orbital period of the isolated low mass protostellar binary system, IRAS 04191+1523, also demonstrates that wide binary systems can be formed by the turbulent fragmentation mechanism, without disk fragmentation/migration. Disk fragmentation and tidal evolution by cluster members cannot explain the existence of this pair either because the stellar density in Taurus is too low³⁰ to alter their orbital parameters. The timescale for the tidal evolution in Taurus is on the order of a few crossing times⁶, or about 100 Myr, much longer than the age of this system. The crossing time for a low density cluster with the stellar initial half-mass radius of 2.53 pc and the initial average velocity dispersion of 0.3 km s^{-1} , which are similar to the conditions in Taurus, is 17 Myrs³¹. Therefore, our high resolution ALMA observations of IRAS 04191+1523 imply that wide binaries in a large range of mass even down to substellar regime can be formed by turbulent fragmentation although parameter spaces for very low mass turbulent cores have not been yet explored by theoretical calculations^{4,5,8}.

METHODS

ALMA observations

IRAS 04191+1523 was observed using the Atacama Large Millimeter/submillimeter Array (ALMA) during Cycle 2 (2013.1.00537.S, PI: Jeong-Eun Lee) on 2015 Jan. 4 and during Cycle 3 (2015.1.00186.S, PI: Michael Dunahm) on 2016 Sep. 28. For the Cycle 2 observation, three spectral windows were centered at 219.5604 GHz ($\text{C}^{18}\text{O } J = 2 \rightarrow 1$), 216.113 GHz ($\text{DCO}^+ J = 3 \rightarrow 2$), and 231.322 GHz ($\text{N}_2\text{D}^+ J = 3 \rightarrow 2$), each with a bandwidth of 58.6 MHz and spectral resolution of 61 kHz ($\Delta v \sim 0.08 \text{ km s}^{-1}$). A continuum window was centered at 234 GHz with a bandwidth of 468.75 MHz. The phase center was at $(\alpha, \delta)_{J2000} = (04^{\text{h}}22^{\text{m}}00.41^{\text{s}}, +15^{\circ}30'21.2'')$, and the total observing time was 54 minutes. Thirty-eight 12-m antennas were used with baselines in the range from 15 m ($\simeq 10 \text{ k}\lambda$) to 350 m ($\simeq 255 \text{ k}\lambda$) to provide the synthesized beam size of $1''.83 \times 1''.26$ (PA= -88.3°) when the natural weighting is adopted.

For the Cycle 3 observation, two continuum windows were centered at 231.1 GHz and 218.5 GHz with a bandwidth of 2 GHz. Two spectral windows were set to cover $\text{CO } J = 2 \rightarrow 1$, $^{13}\text{CO } J = 2 \rightarrow 1$, and $\text{C}^{18}\text{O } J = 2 \rightarrow 1$, but the total observing time (13 minutes) was too short to detect those lines. The phase center was at $(\alpha, \delta)_{J2000} = (04^{\text{h}}22^{\text{m}}00.079^{\text{s}}, +15^{\circ}30'24.833'')$. Forty 12-m antennas were used with baselines in the range from 15 m ($\simeq 11 \text{ k}\lambda$) to 3 km ($\simeq 2327 \text{ k}\lambda$) to provide the synthesized beam size of $0''.24 \times 0''.14$ (PA= $14^\circ.7$) when the uniform weighting is adopted.

We carried out a standard reduction using CASA³² for both data sets. The nearby quasar J0510+1800 was used for phase and flux calibration, and J0423-0120 provided a bandpass calibration for the Cycle 2 data. For the Cycle 3 data, J0510+1800 was used for bandpass and flux calibration while J0407+0742 was used for phase calibration. The visibility data were imaged using the CLEAN algorithm with natural weighting for C¹⁸O to have a higher signal-to-noise ratio while uniform weighting was used for the continuum images to provide higher resolutions. For the Cycle 2 data, the RMS noise levels for C¹⁸O, DCO⁺, and N₂D⁺ are 7, 5, and 8 mJy beam⁻¹, respectively, while the continuum rms noise is 1.0 mJy beam⁻¹. For the Cycle 3 data, the rms noise level for the continuum is 0.45 mJy beam⁻¹.

Disk masses and inclinations

In the 1.3 mm continuum, the disks are unresolved at the lower resolution of $\sim 1.2''$ while they are resolved at the high resolution of $\sim 0.2''$ (see Figure 2 in the main paper). The disk of A is marginally resolved and its deconvolved size is about 26 AU in diameter. The deconvolved disk size of B is about 85 AU in diameter, which is much bigger than the beam size. We use the high resolution images to derive disk properties. Supplementary Table 1 shows the results of Gaussian fitting of the continuum emission. When the emission is optically thin and the dust temperature is constant, the disk mass is calculated by

$$M_{\text{dust}} = \frac{D^2 F}{\kappa_{1.3} B(T_{\text{dust}})}, \quad (1)$$

where D (=140 pc) is the distance to the source, F is the flux density at 1.3 mm, and B is the Planck function at the dust temperature, T_{dust} at 1.3 mm. The assumed dust opacity, commonly

used for disks³³, is $\kappa_{1,3} = 3.5 \text{ cm}^2 \text{ g}^{-1}$.

The deconvolved disk sizes and the inclination of each disk are listed in Supplementary Table 2. The inclination of a disk can be calculated by the size ratio between major and minor axes, $\cos^{-1}(\theta_{\min}/\theta_{\text{maj}})$. The calculated inclinations for A and B are $\sim 55^\circ$ and $\sim 59^\circ$, respectively.

The C¹⁸O emission

Supplementary Figure 1 shows the C¹⁸O spectra extracted from the two disk positions (A and B) and a position (C) in between as marked in Figure 1 of the main paper. The broad wings detected in C¹⁸O trace the disk rotation. The red and blue wing components are shaded as red and blue, where the emission is integrated to demonstrate the disk rotation in Figure 3 of the main paper. For IRAS 04191+1523 B, the blue wing spectrum is flipped on top of the red wing spectrum to show that the red wing is contaminated by an additional component, which is likely the emission from infalling material because C¹⁸O $J = 2 \rightarrow 1$ is a high density tracer. Therefore, we use only the blue wing to determine the Keplerian rotation for protostar B.

The velocity profiles for high velocity wings of IRAS 04191+1523 A and B, respectively, along the white lines in Figure 3 of the main paper are presented in Supplementary Figure 2 in logarithmic scale. In this figure, the X-axis represents the position of peak emission found by Gaussian fitting of the emission distribution along the white line in Figure 3 at a given velocity. The best-fit power-law profiles to the data have power indices similar to the value (0.5) for the Keplerian rotation; the scatter could be caused by/from contamination of other gas motions such

as infall. As a result, we applied the Keplerian rotation to their velocity profiles to derive the masses of two protostars (see Figure 4 in the main paper.) The masses after correction for disk inclination are 0.14 and 0.12 M_{\odot} , for protostars A and B, respectively (see Supplementary Table 3). With these masses, we can test the stability of this protostellar binary system¹⁴. When the velocity difference of two sources is $\sim 0.1 \text{ km s}^{-1}$ (similar to the velocity resolution of the C^{18}O observation) and the projected separation is considered as the actual separation, the ratio of kinetic energy to gravitation energy is about 0.04 and 0.05 for protostars A and B, respectively, indicating that this binary is likely bound.

The projected position angles of two disks were determined using channel maps as presented in Supplementary Figure 3. The blue- and red-shifted components from the source velocity (v_s) by the amounts indicated above each panel are presented as contours. In each channel, the positions of the blue- and red-shifted emission peaks were connected to determine the position angle. The mean and standard deviation of the position angles for velocity shifts between $v_s \pm 0.9$ and $v_s \pm 1.4$ are listed in Supplementary Table 1. The difference in the projected position angles of the two disks is about 77° . The true position angle difference depends on projection; if we consider the disk inclinations derived from the continuum images, the position angle difference of the two disks in space is $63 \pm 5.8^\circ$ or $98 \pm 5.5^\circ$ depending on the direction of two disk inclinations.

Data Availability

The data that support the plots within this paper and other findings of this study are available from ALMA archives with project codes 2013.1.00537.S (https://almascience.nao.ac.jp//aq/?project_code=2013.1

and 2015.1.00186.S (http://almascience.nao.ac.jp//aq/?project_code=2015.1.00186.S) and from the corresponding author upon reasonable request.

References

1. Béjar, V. J. S. *et al.* Discovery of a Wide Companion near the Deuterium-burning Mass Limit in the Upper Scorpius Association. *Astrophys. J. Letters* **673**, L185 (2008). 0712.3482.
2. Luhman, K. L., Mamajek, E. E., Allen, P. R., Muench, A. A. & Finkbeiner, D. P. Discovery of a Wide Binary Brown Dwarf Born in Isolation. *Astrophys. J.* **691**, 1265–1275 (2009). 0902.0425.
3. Luhman, K. L. The Formation and Early Evolution of Low-Mass Stars and Brown Dwarfs. *Ann. Rev. Astron. Astrophys.* **50**, 65–106 (2012). 1208.5800.
4. Goodwin, S. P., Whitworth, A. P. & Ward-Thompson, D. Simulating star formation in molecular cloud cores. I. The influence of low levels of turbulence on fragmentation and multiplicity. *Astron. & Astrophys.* **414**, 633–650 (2004). astro-ph/0309829.
5. Fisher, R. T. A Turbulent Interstellar Medium Origin of the Binary Period Distribution. *Astrophys. J.* **600**, 769–780 (2004). astro-ph/0303280.
6. Marks, M. & Kroupa, P. Inverse dynamical population synthesis. Constraining the initial conditions of young stellar clusters by studying their binary populations. *Astron. & Astrophys.* **543**, A8 (2012). 1205.1508.

7. Dunham, M. M. *et al.* The Spitzer c2d Survey of Nearby Dense Cores. I. First Direct Detection of the Embedded Source in IRAM 04191+1522. *Astrophys. J.* **651**, 945–959 (2006). astro-ph/0607665.
8. Offner, S. S. R., Kratter, K. M., Matzner, C. D., Krumholz, M. R. & Klein, R. I. The Formation of Low-mass Binary Star Systems Via Turbulent Fragmentation. *Astrophys. J.* **725**, 1485–1494 (2010). 1010.3702.
9. Kratter, K. M., Matzner, C. D., Krumholz, M. R. & Klein, R. I. On the Role of Disks in the Formation of Stellar Systems: A Numerical Parameter Study of Rapid Accretion. *Astrophys. J.* **708**, 1585–1597 (2010). 0907.3476.
10. Bate, M. R. Stellar, brown dwarf and multiple star properties from a radiation hydrodynamical simulation of star cluster formation. *MNRAS* **419**, 3115–3146 (2012). 1110.1092.
11. Dunham, M. M. *et al.* The Evolution of Protostars: Insights from Ten Years of Infrared Surveys with Spitzer and Herschel. *Protostars and Planets VI* 195–218 (2014). 1401.1809.
12. Tobin, J. J. *et al.* The VLA Nascent Disk and Multiplicity Survey of Perseus Protostars (VANDAM). II. Multiplicity of Protostars in the Perseus Molecular Cloud. *Astrophys. J.* **818**, 73 (2016). 1601.00692.
13. Tobin, J. J. *et al.* A triple protostar system formed via fragmentation of a gravitationally unstable disk. *Nature* **538**, 483–486 (2016). 1610.08524.
14. Pineda, J. E. *et al.* The formation of a quadruple star system with wide separation. *Nature* **518**, 213–215 (2015).

15. Offner, S. S. R., Dunham, M. M., Lee, K. I., Arce, H. G. & Fielding, D. B. The Turbulent Origin of Outflow and Spin Misalignment in Multiple Star Systems. *Astrophys. J. Letters* **827**, L11 (2016). 1606.08445.
16. Bonnell, I. A. & Bate, M. R. Massive Circumbinary Discs and the Formation of Multiple Systems. *MNRAS* **269** (1994).
17. Lee, J. W. Y., Hull, C. L. H. & Offner, S. S. R. Synthetic Observations of Magnetic Fields in Protostellar Cores. *Astrophys. J.* **834**, 201 (2017). 1611.08530.
18. Jensen, E. L. N., Mathieu, R. D., Donar, A. X. & Dullighan, A. Testing Protoplanetary Disk Alignment in Young Binaries. *Astrophys. J.* **600**, 789–803 (2004).
19. Jensen, E. L. N. & Akeson, R. Misaligned protoplanetary disks in a young binary star system. *Nature* **511**, 567–569 (2014). 1407.8211.
20. Salyk, C. *et al.* ALMA Observations of the T Tauri Binary System AS 205: Evidence for Molecular Winds and/or Binary Interactions. *Astrophys. J.* **792**, 68 (2014). 1407.2652.
21. Williams, J. P. *et al.* ALMA Observations of a Misaligned Binary Protoplanetary Disk System in Orion. *Astrophys. J.* **796**, 120 (2014). 1410.3570.
22. Duchêne, G., Bouvier, J., Bontemps, S., André, P. & Motte, F. Multiple protostellar systems. I. A deep near infrared survey of Taurus and Ophiuchus protostellar objects. *Astron. & Astrophys.* **427**, 651–665 (2004). astro-ph/0407482.

23. Luhman, K. L., Allen, P. R., Espaillat, C., Hartmann, L. & Calvet, N. The Disk Population of the Taurus Star-Forming Region. *Astrophys. J. Suppl.* **186**, 111–174 (2010). 0911.5457.
24. Connelley, M. S., Reipurth, B. & Tokunaga, A. T. The Evolution of the Multiplicity of Embedded Protostars. I. Sample Properties and Binary Detections. *Astron. J.* **135**, 2496–2525 (2008). 0803.1656.
25. Dang-Duc, C., Phan-Bao, N. & Dao-Van, D. T. Two confirmed class I very low-mass objects in Taurus. *Astron. & Astrophys.* **588**, L2 (2016). 1602.06357.
26. Bulger, J. *et al.* The Taurus Boundary of Stellar/Substellar (TBOSS) Survey. I. Far-IR disk emission measured with Herschel. *Astron. & Astrophys.* **570**, A29 (2014). 1407.4802.
27. Tobin, J. J. *et al.* A ~ 0.2 -solar-mass protostar with a Keplerian disk in the very young L1527 IRS system. *Nature* **492**, 83–85 (2012). 1212.0861.
28. Young, C. H. *et al.* Submillimeter Common-User Bolometer Array Mapping of Spitzer c2d Small Clouds and Cores. *Astron. J.* **132**, 1998–2013 (2006). astro-ph/0609206.
29. André, P., Motte, F. & Bacmann, A. Discovery of an Extremely Young Accreting Protostar in Taurus. *Astrophys. J. Letters* **513**, L57–L60 (1999).
30. Rebull, L. M. *et al.* The Taurus Spitzer Survey: New Candidate Taurus Members Selected Using Sensitive Mid-Infrared Photometry. *Astrophys. J. Suppl.* **186**, 259–307 (2010). 0911.3176.

31. Kroupa, P. Inverse dynamical population synthesis and star formation. *MNRAS* **277** (1995). astro-ph/9508117.
32. McMullin, J. P., Waters, B., Schiebel, D., Young, W. & Golap, K. CASA Architecture and Applications. In Shaw, R. A., Hill, F. & Bell, D. J. (eds.) *Astronomical Data Analysis Software and Systems XVI*, vol. 376 of *Astronomical Society of the Pacific Conference Series*, 127 (2007).
33. Andrews, S. M. & Williams, J. P. Circumstellar Dust Disks in Taurus-Auriga: The Submillimeter Perspective. *Astrophys. J.* **631**, 1134–1160 (2005). astro-ph/0506187.

Acknowledgements This paper makes use of the following ALMA data: ADS/JAO.ALMA#2013.1.00537.S, and 2015.1.00186.S. ALMA is a partnership of ESO (representing its member states), NSF (USA) and NINS (Japan), together with NRC (Canada), and NSC and ASIAA (Taiwan), and KASI (Republic of Korea), in cooperation with the Republic of Chile. The Joint ALMA Observatory is operated by ESO, AUI/NRAO and NAOJ. J.-E. Lee was supported by the Basic Science Research Program through the National Research Foundation of Korea (NRF) (grant No. NRF-2015R1A2A2A01004769) and the Korea Astronomy and Space Science Institute under the R&D program (Project No. 2015-1-320-18) supervised by the Ministry of Science, ICT and Future Planning. NJE thanks KASI for support for a visit to participate in this work.

Author Contributions JEL and SL performed the detailed calculations used in the analysis. SL and KT reduced the ALMA data. JEL wrote the manuscript. All authors were participants in the discussion of results, determination of the conclusions, and revision of the manuscript.

Competing Interests The authors declare that they have no competing financial interests.

Correspondence Correspondence and requests for materials should be addressed to Jeong-Eun Lee (email: jeongeun.lee@khu.ac.kr).

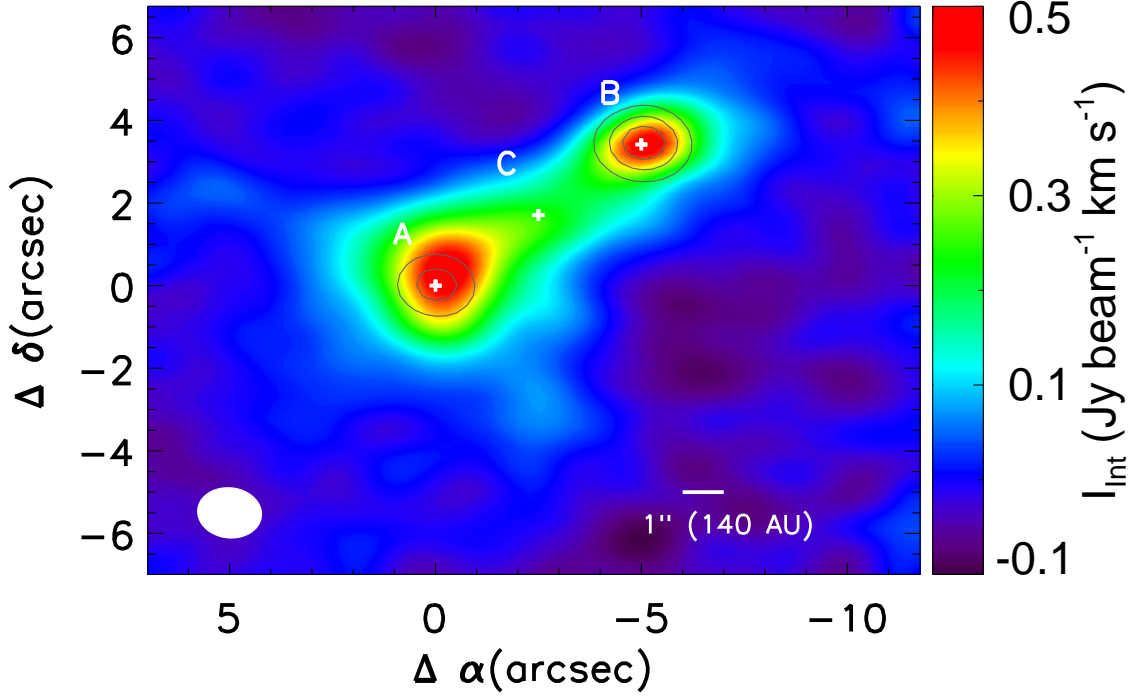


Figure 1: Two compact continuum sources detected in the 1.3 mm continuum (black contours) on top of the C^{18}O J=2-1 integrated intensity (colour image). The lowest contour and subsequent contour step are 20 times the rms noise of $1.0 \text{ mJy beam}^{-1}$. A and B indicate the positions of protostars. More extended C^{18}O emission exists around A although the 1.3 mm continuum emission is stronger around B. C represents a common envelope position not associated with compact continuum emission. The peak intensities (and their 1σ error) of the two continuum sources, which are measured with the task *imfit* in CASA, are $51 (\pm 0.9)$ and $76 (\pm 1.0) \text{ mJy beam}^{-1}$, respectively.

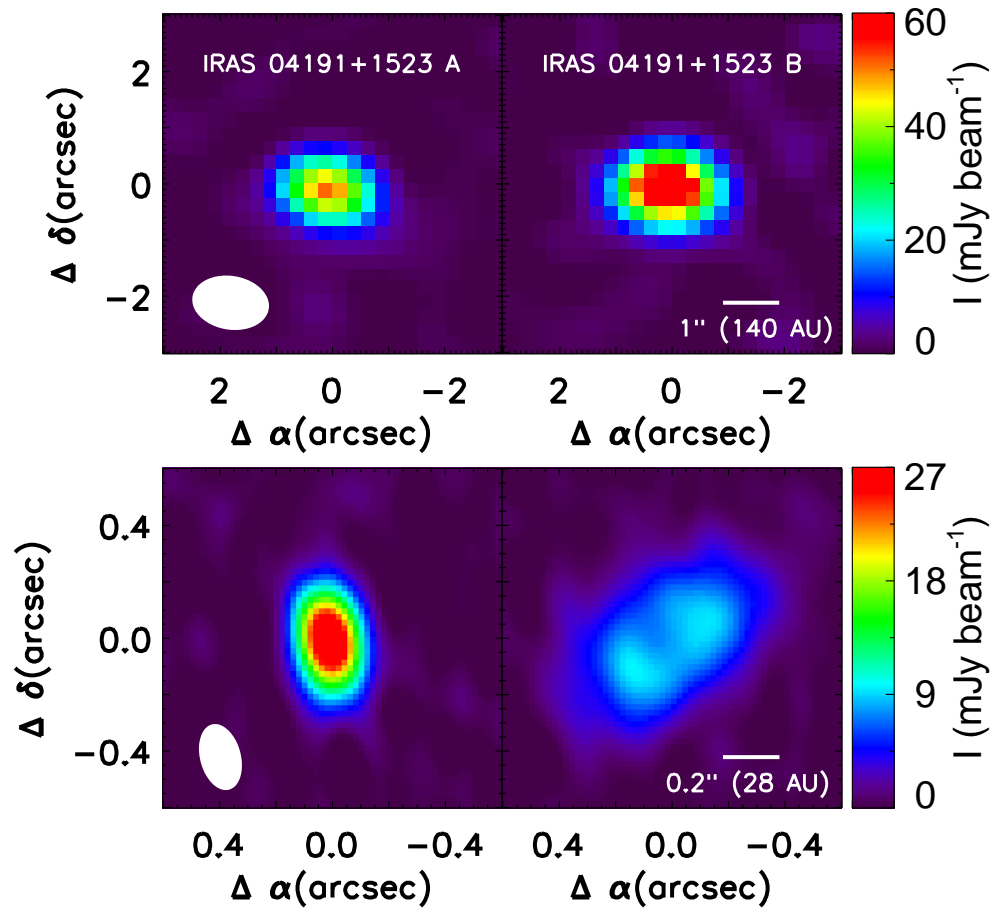


Figure 2: Continuum images in two different resolutions. The upper and lower panels show the 1.3 mm continuum images in the resolutions of $\sim 1.2''$ and $\sim 0.2''$, respectively, when the uniform weighting is adopted. In the higher resolution images, two continuum sources are resolved as disks (see the text and Supplementary Table 1 and 2).

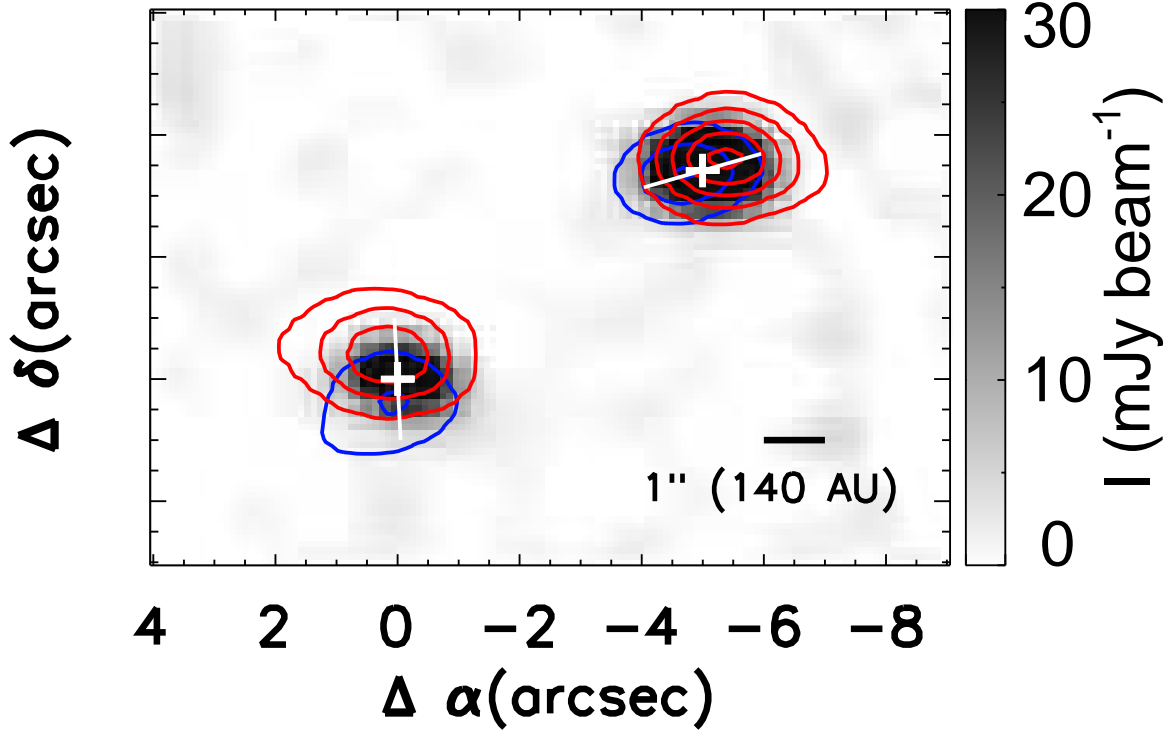


Figure 3: Protostellar binary disks detected in the high velocity wings of the $\text{C}^{18}\text{O } J = 2 \rightarrow 1$ emission line on top of the continuum image (gray scale). The red and blue components are integrated in the velocity ranges from 7.65 to 9.15 km s^{-1} and from 4.35 to 5.85 km s^{-1} , respectively. The lowest contour and subsequent contour step are 10 times the rms noise of $2.4 \text{ mJy beam}^{-1} \text{ km s}^{-1}$. The white lines connect the blue- and red-shifted emission peaks, and thus, they are considered to be perpendicular to the disk rotation axes. The peak-position-velocity diagrams, presented in Figure 4, are obtained along these lines.

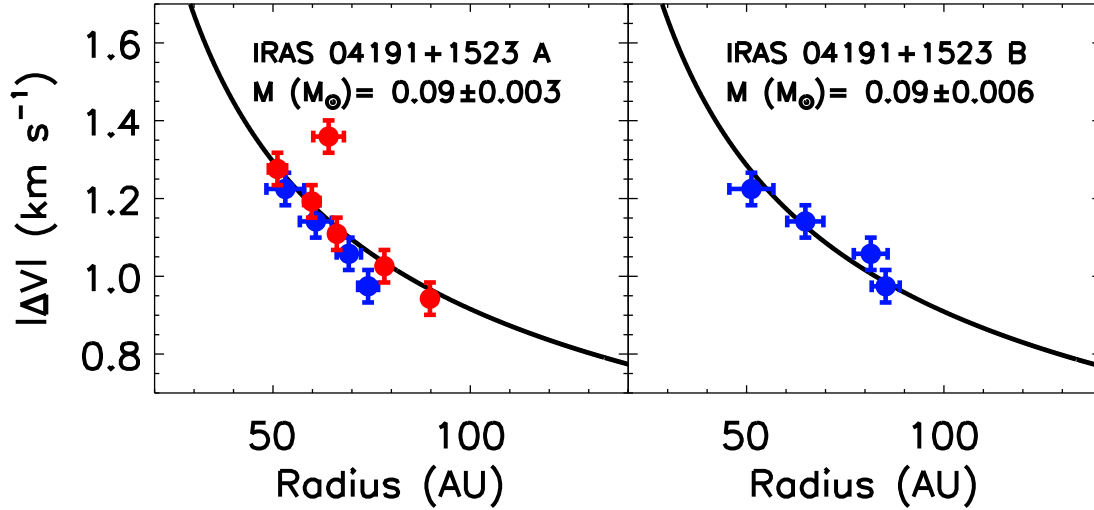
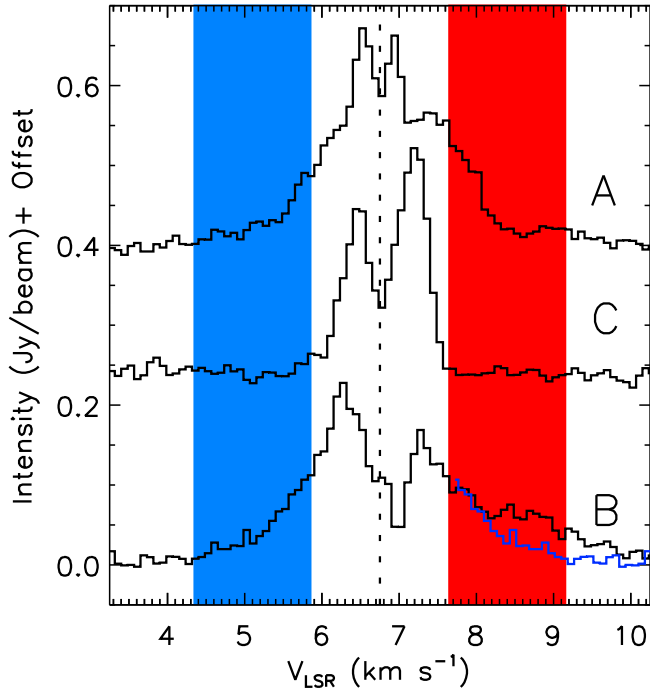
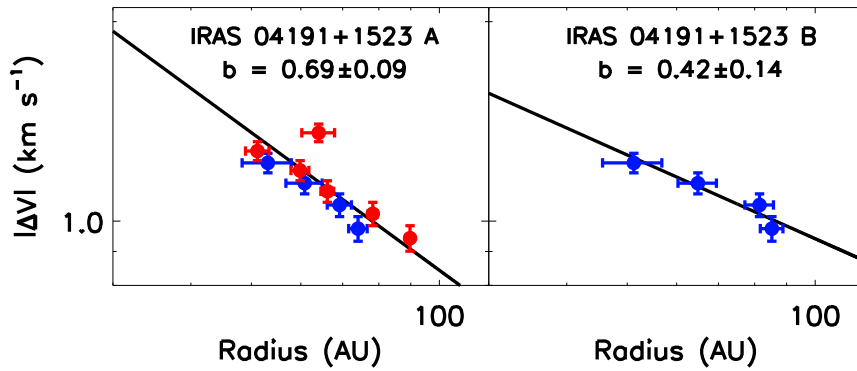


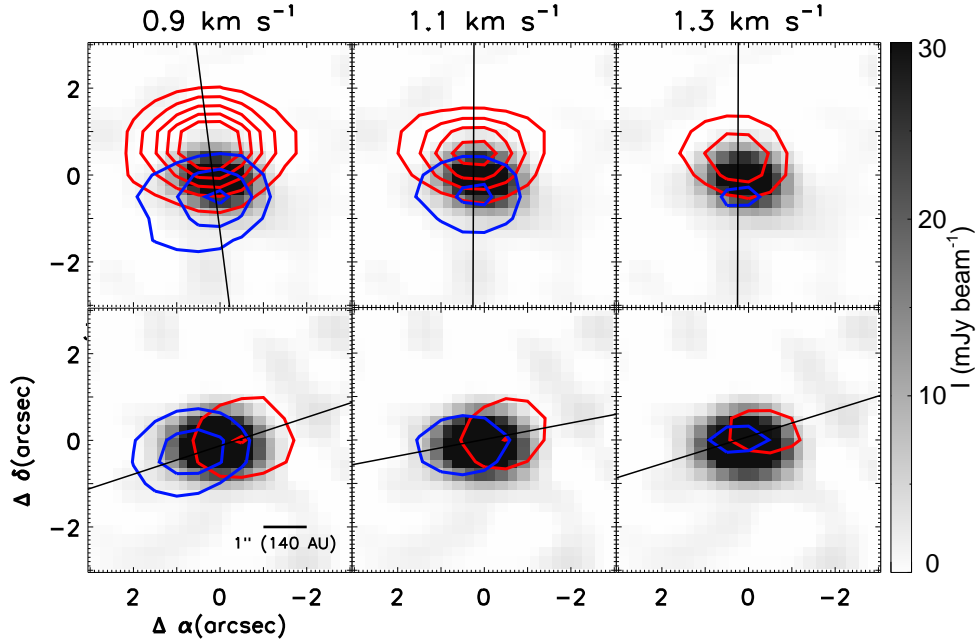
Figure 4: The velocity profiles for high velocity wings of IRAS 04191+1523 A and B, respectively, along the white lines in Figure 3. Only blue shifted velocities are plotted for B because the red shifted emission is contaminated by an additional component (see Supplementary Figure 1). The source velocity is found from the spectrum at the position C in Figure 1 (see Supplementary Figure 1), as 6.75 km s^{-1} , in which the velocity profiles for red and blue-shifted wings of IRAS 04191+1523 A are consistent without displacement as seen in the figure. The solid curves represent the best-fit Keplerian velocity profiles with the central mass of $0.09 M_{\odot}$ for both sources when an edge-on view is assumed. The vertical error bars represent the velocity resolution ($\sim 0.08 \text{ km s}^{-1}$), and the horizontal error bars indicate the 1σ error in the position of emission peak, which is derived by Gaussian fitting of the C^{18}O emission distribution along the white lines marked in Figure 3 at a given velocity channel.



Supplementary Figure 5: The C^{18}O spectra for the two disk positions and in between the two disks (position C in figure 1 of the main paper). The spectrum at C represents the common envelope with no disk emission. Therefore, we define the velocity ranges (shaded as blue and red) for the disk emission based on this spectrum. The blue line above 7.65 km s^{-1} at the position B indicates the spectrum of the blue wing reflected about the source velocity of 6.75 km s^{-1} , which is marked with the dashed line. It shows an additional bump in the red wing at the position B. A Gaussian fit places the additional component at 8.9 km s^{-1} .



Supplementary Figure 6: The velocity profiles for the high velocity wings of IRAS 04191+1523 A and B, respectively, in logarithmic scale. The data points and error bars are the same as in Figure 4. When the velocity profile follows a power-law function with radius ($|\Delta V| \propto r^{-b}$), the least squares fitting method show the best-fit power indices (and their uncertainties) of A and B are 0.69 (± 0.09) and 0.42 (± 0.14), respectively. These values are similar to the power index (0.5) for the Keplerian rotation.



Supplementary Figure 7: The channel maps of high velocity components of the C^{18}O emission for IRAS 04191+1523 A (top) and B (bottom) on top of the continuum image (gray scale). The lowest contour and subsequent contour step are 5 times the rms noise, which is $6.9 \text{ mJy beam}^{-1}$ and $10.9 \text{ mJy beam}^{-1}$ for A and B, respectively. The thin black line marked in each box connects the blue- and red-shifted emission peaks. The mean and standard deviation of the position angles measured from the thin black lines are $2.9 \pm 4.1^\circ$ and $-74.0 \pm 6.1^\circ$. The velocity marked at the top of each column indicates the velocity shifted from the source velocity.

Supplementary Table 1: Source Properties of IRAS 04191+1523

	R.A.	Dec.	Continuum Flux density	Continuum Peak Intensity	Disk mass ^a
			mJy	mJy beam ⁻¹	$\times 10^{-3} M_{\odot}$
A	04:22:00.4283	+15:30:21.189	53.5	33.1	3.70
	(0''.001)	(0''.002)	(1.1)	(0.46)	(0.08)
B	04:22:00.0826	+15:30:24.605	71.1	10.2	4.91
	(0''.001)	(0''.009)	(3.2)	(0.41)	(0.22)

The continuum flux density and peak intensity are measured with the task, imfit in CASA. The value in parenthesis is the error (1σ).

^aThe disk mass is calculated by the equation (1) in Methods.

Supplementary Table 2: Deconvolved Disk Sizes and Inclinations of IRAS 04191+1523

	θ_{maj}^a	θ_{min}^a	$\theta_{\text{incl.}}^b$	<i>P.A.</i>
	mas	mas	°	°
A	189.3 (9.0)	109.4 (5.4)	54.6 (2.8)	0.0 (3.9)
B	608 (29)	309 (20)	59.3 (2.7)	-55.2 (3.1)

These are measured with the CASA task, imfit. The value in the parenthesis is the error (1σ).

The synthesized beam is $0''.24 \times 0''.14$ (P.A. = 14.72).

^aFWHM of major and minor axes.

^b $\theta_{\text{incl.}} = \cos^{-1}(\theta_{\text{min}}/\theta_{\text{maj}})$.

Supplementary Table 3: Protostellar mass derived by Keplerian rotation velocity profile

	Minimum mass ^a	Actual mass ^b
	M_{\odot}	M_{\odot}
A	0.09 (0.003)	0.14 (0.01)
B	0.09 (0.006)	0.12 (0.01)

^a Protostellar mass derived assuming edge-on disk.

^b Protostellar mass corrected for inclination (see Supplementary Table 2).